Estimation of internal tide energy available for deep ocean mixing based on three-dimensional global numerical simulations

Yoshihiro Niwa and Toshiyuki Hibiya

Department of Earth and Planetary Science, Graduate School of Science,

The University of Tokyo, Bunkyo-ku, Tokyo 113-0033, Japan

Authors' information:

Y. Niwa and T. Hibiya, Department of Earth and Planetary Science, Graduate School of Science, The University of Tokyo, 7-3-1, Hongo, Bunkyo-ku, Tokyo 113-0033, Japan (e-mail: niwa@eps.s.u-tokyo.ac.jp)

Abstract

The global distributions of the major semidiurnal (M_2 and S_2) and diurnal (K_1 and O_1) internal tide energy are investigated using a hydrostatic sigma-coordinate numerical model. A series of numerical simulations using various horizontal grid spacings of 1/15° -1/5° shows that generation of energetic internal tides is restricted over representative prominent topographic features. For example, nearly half of the diurnal (K_1 and O_1) internal tide energy is excited along the western boundary of the North Pacific from the Aleutian Islands down to the Indonesian Archipelago. It is also found that the rate of energy conversion from the surface tide to internal tides is very sensitive to the horizontal grid spacing as well as the resolution of the model bottom topography; the conversion rate integrated over the global ocean increases exponentially as the model grid spacing is reduced. Extrapolating the calculated results in the limit of zero grid spacing yields the estimate of the global conversion rate to be 1105GW (821GW, 145GW, 102GW, 53GW for M_2, S_2, K_1, and O_1 tidal constituents, respectively). The amount of internal tide energy dissipated in the open ocean below a depth of 1000m, in particular, is estimated to be 500-600GW, which is comparable to the mixing energy estimated by Webb and Suginohara (2001) as needed to sustain the global overturning circulation.

Keywords:
Internal tide, Deep ocean mixing, Global overturning circulation

1. Introduction

Internal (baroclinic) tides are ubiquitous phenomena in the stratified ocean. They are generated by surface (barotropic) tidal currents flowing over rough ocean bottom such as mid-ocean ridge and continental shelf slope; the stratified water is then vertically up and down and part of the surface tide energy is converted into internal tide energy. Internal tides have large vertical displacement of density surfaces in the ocean interior with amplitudes reaching several tens of meters and are characterized by relatively short horizontal wavelengths of the order of 100 km.

Internal tides have strong influences on the global overturning circulation and hence on the world's climate, because they are thought to contribute to turbulent mixing in the deep ocean; near the generation sites, the vertical shear of horizontal currents associated with internal tides can be strong enough to cause shear instability leading to locally enhanced turbulent mixing. Turbulent mixing can also be induced even far from the generation sites, because propagating internal tides nonlinearly interact with the background internal waves and/or mesoscale eddies and cascade part of their energy down to small dissipation scales inducing shear instability. The induced turbulent mixing transfers heat from the surface down to the dense deep water that originates from high latitudes, causing it to upwell back to the sea surface at low and mid latitudes. Actually, ocean general circulation models (OGCMs) (e.g. Hasumi and Suginohara, 1999) demonstrate that the rate and spatial distribution of turbulent mixing can strongly control the fundamental features of the global overturning circulation such as flow and

density structures as well as the transports of heat and chemical tracers. Thus, understanding the global distribution of internal tide energy is essential for accurate modeling of the ocean general circulation.

Accurate estimates of internal tide energy are also crucial for understanding the energy balance of the global overturning circulation. Munk and Wunsch (1998) estimated that 2100GW (1GW=10^9W) of the mixing energy is required to pull up 30Sv of the dense deep water below a depth of 1000m (the typical depth of the main thermocline) and postulated nearly half of which was supplied by internal tides and the remaining half by the wind-induced internal waves. On the other hand, Webb and Suginohara (2001) suggested that the Ekman suction in the Southern Ocean might pull up about half of the deep water formed in the North Atlantic to the sea surface, reducing the required mixing energy as low as 600GW. It still remains a matter of debate which of these mixing energy analyses is more convincing (Kuhlbrodt et al., 2007). An important step to answer this question is to accurately estimate the amount of internal tide energy available for deep ocean mixing.

Many studies have been carried out to predict the global distribution of the rate of energy conversion from the surface tide to internal tides (Sjöberg and Stigebrandt, 1992; Morozov, 1995; Kantha and Tierney, 1995; Jayne and St. Laurent, 2001; Nycander, 2005). However, estimates of the global baroclinic conversion rate derived from these studies vary widely (more than ±50%), because they are based on simplified analytical models under idealized assumptions whose applicability to the real ocean is

questionable. Using the TOPEX/Poseidon altimetry data and an inverse tidal model, on the other hand, Egbert and Ray (2001) estimated that roughly 1000GW or 20-30% of the global surface tide energy is dissipated within the open ocean including the region of rough seafloor topography. But their inverse tidal model cannot discriminate between the dissipation due to internal tide generation and the direct frictional dissipation within bottom boundary layer (BBL). Thus, to accurately estimate the internal tide energy available for deep ocean mixing, numerical studies based on the primitive Navier-Stokes equations are most desirable. Up until today, only one numerical study attempting to simulate the global internal tide field has been carried out by Simmons et al.(2004), but they were concerned only with the most dominant M_2 tidal response for a horizontally uniform idealized density stratification. Furthermore, vertical grid resolutions in their numerical model (2 or 10 layers) are too coarse to adequately resolve high vertical-mode internal tides.

In the present study, we investigate the spatial distribution of the major semidiurnal (M_2 and S_2) and diurnal (K_1 and O_1) internal tide energy using a fine-grid three-dimensional numerical model incorporating the realistic bottom topography, density stratification, and barotropic tidal forcing. In order to accurately estimate the rate of energy conversion into internal tides, in particular, a series of numerical simulations with various horizontal grid spacings of 1/5˚-1/15˚ is conducted to examine the sensitivity of the calculated results to the model grid spacing as well as the resolution of the model bottom topography.

2. Numerical Experiment

Figure 1 shows the model domain that covers the global ocean from 80˚S to 80˚N, excluding the central part of the Arctic Ocean and the shallow shelf regions near the Antarctic continent.

The governing equations are the full three-dimensional Navier-Stokes equations under hydrostatic and Boussinesq approximations. The vertical eddy viscosity and diffusivity are parameterized following the Richardson-number formulation of Pacanowski and Philander (1981). Furthermore, taking into account the decay of propagating internal tides due to their nonlinear interactions with the background Garrett-Munk internal waves (Munk, 1981) as well as mesoscale eddies, we include artificial linear damping terms for the depth-varying horizontal velocities and the deviations of potential temperature and salinity from the basic fields. In the present study, the damping time is set to be 30 days which is estimated based on the analysis of tidal current data obtained from long-term mooring observations (the details of the data analysis will be reported elsewhere).

The governing equations are numerically integrated using the Princeton Ocean Model (Blumberg and Mellor, 1987). To examine the sensitivity of the model results to the horizontal grid spacing as well as the resolution of the model bottom topography, a set of numerical experiments is carried out using five different horizontal grid spacings, namely, 1/5˚, 1/6˚, 2/15˚, 1/10˚, and 1/15˚. In all the cases, 41 sigma levels are assumed in the vertical with a logarithmic distribution near the sea surface. For the details of the

governing equations and the numerical model, readers are referred to Niwa and Hibiya (2004).

For each numerical experiment, the model topography is constructed by averaging the 2-minute (1/30˚) gridded global bathymetric data of ETOPO2 (Smith and Sandwell, 1997) within each model grid cell. The basic temperature and salinity fields are obtained from the annual mean data of National Ocanographic Data Center's World Ocean Atlas (Levitus and Boyer, 1994; Levitus et al., 1994).

The model is forced by the tidal potential forcing of four major semidiurnal and diurnal astronomical tidal constituents (M_2, S_2, K_1 and O_1). Furthermore, in order to reproduce the realistic surface tidal field, we assimilate the surface tidal elevation data of Matsumoto et al. (2000). The model is driven by the M_2, S_2, K_1 and O_1 tidal forcing for 60 days from an initial state of rest with time steps of 30 sec and 3.75 sec for the baroclinic and barotropic modes, respectively. The calculated timeseries data for the last 20 days are harmonically analyzed to obtain the amplitude and phase of each tidal constituent. In order to extract the information about internal tides, we subtract the depth-averaged tidal currents from the calculated tidal currents.

3. Results

Figure 2(a) shows the global distribution of the depth-integrated kinetic energy of the semidiurnal (M_2 and S_2) internal tides obtained using the finest horizontal grid spacing of 1/15˚. It should be noted that, unless otherwise stated, the calculated results using the

finest horizontal grid (1/15°) will be shown hereafter, because the qualitative features are the same for all the other results using the coarser horizontal grids. Figure 2(a) indicates that the spatial distribution of the semidiurnal internal tide energy is highly inhomogeneous reflecting that of the prominent topographic features. Particularly high energy levels are found in the western Pacific Ocean, the western Indian Ocean and the Mid-Atlantic Ocean, which are 2-3 orders of magnitude higher than those in the Southern Ocean and the eastern Pacific Ocean.

To examine the generation of internal tides more quantitatively, we calculate the depth-integrated energy conversion rate from the surface tide to internal tides (Niwa and Hibiya, 2004) defined as

$$C(x,y) \equiv \int_{-H}^{0} g\overline{\rho' w_s} dz \qquad (1)$$

where H is the total depth of the water column, g is the acceleration due to gravity, ρ' is the density deviation from the basic field associated with internal tide motions, w_s is the vertical velocity resulting from the interaction of depth-averaged tidal currents with bottom topographic features, and the overbar denotes the temporal average over one tidal period. In Figure 3, the depth-integrated energy conversion rate from the surface tide to internal tides is further integrated within each 5°-latitude by 5°-longitude grid area to identify the important generation regions.

We can see in Figure 3(a) that the semidiurnal internal tides are effectively generated in the coastal and marginal seas such as over the prominent topographic features in the Indonesian Archipelago and over the continental shelf slope in the East China Sea and

the Andaman Sea. Energetic internal tides can be generated also in the open ocean along the steep topographic features such as the Hawaiian Ridge, the Izu-Ogasawara Ridge, the Western-Indian Ridges, and the Mid-Atlantic Ridges, and over the seamounts in the Micronesia Islands and the Polynesia Islands.

Figure 2(b) shows the spatial distribution of the diurnal (K_1 and O_1) internal tide energy. We can see that the diurnal internal tide energy is mostly limited equatorward of about 30˚N/S, because each linear diurnal internal tide cannot propagate freely poleward of the critical latitude where the diurnal tidal frequency becomes subinertical (the exact critical latitudes for K_1 and O_1 internal tides are 30.00˚N/S and 27.37˚N/S, respectively). Energetic diurnal internal tides are also excited at high latitudes beyond the critical latitudes in the form of coastal-trapped waves propagating along the steep topographic features in the Aleutian Islands and the Kuril Islands. Figure 3(b) shows that the generation of large diurnal internal tides is mostly limited along the western boundary of the North Pacific from the Aleutian Islands down to the Indonesian Archipelago where nearly half of the global diurnal internal tide energy is found to be excited.

The rate of energy conversion from the surface tide to internal tides integrated over the global ocean is estimated to be 782GW (553GW, 96GW, 87GW, 46GW for M_2, S_2, K_1, and O_1 tidal constituents, respectively) for the finest horizontal grid (1/15˚). This value does not change appreciabley even if the linear damping time scale is changed or the annual mean temperature and salinity fields are replaced by the corresponding summer/winter climatological fields. The global baroclinic conversion rate is, however,

very sensitive to the horizontal grid spacing and hence the resolution of the model bottom topography (Table 1); increasing the horizontal grid spacing from 1/15° to 1/5° leads to the decrease of the global conversion rate from 782GW to 394GW. Figure 4 plots the global conversion rate on a logarithm scale against the horizontal grid spacing, showing that the logarithm of the conversion rate increases linearly as the horizontal grid spacing is reduced. This is consistent with the similar relationship found between the globally integrated power of the slope of the bottom topographic features $\left(\int(\nabla H)^2 dxdy\right)$ used for each numerical experiment and the horizontal grid spacing (Figure 5). Extrapolating the least-square fitting in the limit of zero grid spacing (see Figure 3), we can estimate the global baroclinic conversion rate to be 1105GW (821GW, 145GW, 102GW, 53GW for M_2, S_2, K_1, and O_1 tidal constituents, respectively) (Table 1) which corresponds to 32% of the global tidal energy dissipation rate of 3500GW.

It should be noted, however, that thus estimated global internal tide energy is not fully available to sustain the global overturning circulation, because turbulent mixing that occurs in the coastal and marginal seas and/or in the upper ocean above the main thermocline does not come into play in pulling up the dense deep water that originates from high latitudes. Therefore, to evaluate the amount of internal tide energy available for deep ocean mixing needed to sustain the global overturning circulation, we have to estimate how much of the internal tide energy propagates outward into the open ocean and dissipates below the main thermocline. For this purpose, we first estimate the depth-integrated dissipation rate of internal tide energy. Assuming nonlinear advection

effect is negligible, it is given by the difference between the energy conversion rate and the energy flux divergence (Niwa and Hibiya, 2004), namely,

$$D(x,y) \equiv \int_{-H}^{0} g\overline{\rho' w_s} dz - \int_{-H}^{0} \left[\frac{\partial}{\partial x}\left(\overline{p'u'}\right) + \frac{\partial}{\partial y}\left(\overline{p'v'}\right) \right] dz \qquad (2)$$

where u', v' and p' are the eastward and northward velocities and the pressure perturbations associated with internal tide motions, respectively. Note that, since the energy fluxes across the northern and southern model boundaries are negligible, the global integral of the energy dissipation rate $\iint_{global} D(x,y)dxdy$ is almost the same as that of the conversion rate $\iint_{global} C(x,y)dxdy$. Figures 6(a) and 6(b) show the spatial distribution of the dissipation rate of the semidiurnal (M_2 and S_2) internal tide energy and that of the diurnal (K_1 and O_1) internal tide energy, respectively. We can see that, although the spatial distribution of the energy dissipation rate is similar to that of the energy conversion rate for each tidal constituent (Figures 3(a) and 3(b)), it spreads outward from each prominent topographic feature as a consequence of internal tide propagation. If the boundary between the open ocean and the coastal and marginal seas is defined as shown by the thick white line in Figure 1, we can extrapolate the total baroclinic dissipation rate within the open ocean (or the coastal and marginal seas) in the limit of zero grid spacing to be 761 (or 345) GW, which is slightly larger (or smaller) than the total baroclinic conversion rate 744 (or 362) GW within the open ocean (or the coastal and marginal seas), which implies that internal tides, on the whole, are carrying their energy from the coastal and marginal seas to the open ocean.

Next, we investigate how much of the internal tide energy is dissipated in the open ocean below a depth of the main thermocline (about 1000m). Recent microstructure measurements (St. Laurent et al., 2002) show that there exists the bottom-intensified turbulent mixing associated with breaking of internal tides, the intensity of which decays upwards within a distance of about 500m from the ocean bottom. Taking into account this, we assume that the depth-integrated dissipation rate $D(x,y)$ is vertically distributed following a vertical structure function given by

$$\phi(z;H)=\frac{e^{-(H+z)/\varsigma}}{\varsigma\left(1-e^{-H/\varsigma}\right)} \qquad (3)$$

which satisfies $\int_{-H}^{0}\phi(z;H)dz=1$. In terms of $\phi(z;H)$, the fraction of internal tide energy that is dissipated in the open ocean at depths greater than $|z|$ can be calculated as

$$F_{open}(z)=\frac{\iint_{open}\left[\int_{-H(x,y)}^{z}D(x,y)\phi(z';H(x,y))dz'\right]dxdy}{\iint_{global}C(x,y)dxdy} \qquad (4)$$

Recent theoretical and observational studies (Iwamae et al., 2009; Decloedt et al., 2010) show that ς in the open ocean can vary from several tens of meters to hundreds meters depending on the characteristic wavelength of small-scale internal tides generated over ocean bottom roughness. Figure 7 shows the plots of $F_{open}(z)$ (thick solid lines) for the scale height parameters ς=10m, 100m, 500m, 1000m, respectively. The same function but for the coastal and marginal seas $F_{coastal}(z)$ is also plotted in Figure 7 (thin dotted line). Although the value of $F_{open}(z)$ at each z decreases as the scale height parameter

ς increases, $F_{open}(z)$ does not change appreciably even if ς is varied over two orders of magnitude. Figure 7 indicates that 45-55 % of the global internal tide energy is dissipated in the open ocean below a depth of 1000m ($F_{open}(-1000m)$). Multiplying this fraction by the global energy conversion rate in the limit of zero grid spacing (1105GW), we can conclude that 500-600 GW of the internal tide energy is supplied to the deep ocean mixing which is available to sustain the global overturning circulation.

4. Summary and Discussions

In the present study, using a three-dimensional numerical model, we have investigated the global distribution and budget of the semidiurnal and diurnal (M_2, S_2, K_1 and O_1) internal tide energy. It has been shown that the semidiurnal internal tide energy becomes particularly high in the western Pacific Ocean, the western Indian Ocean, and the Mid-Atlantic Ocean reflecting the spatial distribution of the prominent topographic features, whereas the diurnal internal tide energy is mostly limited along the western coast of the north Pacific Ocean from the Aleutian Islands down to the Indonesian Archipelago.

The sensitivity experiments have shown that the rate of energy conversion from the surface tide to internal tides strongly depends on the horizontal grid spacing as well as the resolution of the model bottom topography; the energy conversion rate increases exponentially as the horizontal grid spacing is decreased. This clearly indicates the necessity of the numerical simulations with much higher grid resolutions incorporating

fine-scale bathymetric data such as those obtained by multibeam echo sounder observations. Although very high-resolution numerical simulations (horizontal grid spacings less than 1km) incorporating the multibeam bathymetric data have been carried out for the localized regions around the Hawaiian Ridge and/or the Mid-Atlantic Ridges (Carter et al., 2008; Zilberman et al., 2009), such high-resolution numerical simulations cannot extend over the global ocean for the moment due to the insufficient computer capacity as well as the limitation of multibeam bathymetric data.

In the present study, we have instead estimated the baroclinic energy conversion rate in the limit of zero grid spacing by extrapolating the exponential relationship found between the calculated energy conversion rate and the horizontal grid spacing. Figure 8 depicts the schematic diagram showing the global tidal energy budget obtained from the present study. We have found that the global surface tidal energy 3500 GW is converted into internal tide energy 1105GW over the prominent topographic features in the global ocean, and about 750GW of which is dissipated within the open ocean (defined as the region outside the coastal and marginal seas).

We have also found that 45-55 % of the global internal tide energy is dissipated below a depth of 1000m (the typical depth of the main thermocline) in the open ocean so that 500-600GW of internal tide energy is estimated to be available for deep ocean mixing. This value is just barely 30% of 2100GW, namely, the energy required to sustain the global overturning circulation estimated by Munk and Wunsch (1998), while it is consistent with the estimate by Webb and Suginohara (2001) who insisted that the

required mixing energy can be reduced down to 600GW by considering the existence of the Ekman suction in the Southern Ocean adiabatically pulling up about half of the North Atlantic Deep Water (NADW).

Munk and Wunsch (1998) have argued that the remaining energy for deep ocean mixing could be supplied by the wind-induced internal waves. However, recent numerical simulations by Furuichi et al. (2009) and Zhai et al. (2010) both demonstrated that the total wind-induced near-inertial wave energy available for deep ocean mixing was limited to, at most, 100 GW, because more than 70 % of the wind-induced near-inertial wave energy was dissipated within the top 200 m and hence not available for turbulent mixing at greater depths. Even adding the contribution from the wind-induced internal waves, therefore, they estimated the total energy available for deep ocean mixing to be 600-700GW. This seems to support the validity of the argument of Webb and Suginohara (2001) rather than that of Munk and Wunsch (1998).

Alternatively, this might suggest the existence of "missing energy sources" for deep ocean mixing such as internal waves generated by geostrophic flows interacting with topographic features, internal waves generated through geostrophic adjustment processes, and stiring of the water column by swimming animals in the ocean (Ferrari and Wunsch, 2009). Another possibility is that the upwelling transport rate of dense deep water ~30Sv assumed by Munk and Wunsch (1998) might be overestimated. Actually, Schmitz (1995) suggested a much lower value of 14-17Sv. To close the deep global water-mass budget, therefore, accurate estimate of the upwelling transport rate of

dense deep water is necessary besides the search for the energy sources for “missing mixing”.

Finally, it should be pointed out that the budget of the global internal tide energy presented in this study is completely based on the empirical relationship found between the baroclinic conversion rate and the horizontal grid spacing. To ensure the validity of the present study, the physical background behind this empirical relationship should be clarified, which also remains to be studied in the future.

References

Blumberg, A. F. and G. L. Mellor (1987): A description of a three-dimensional coastal ocean circulation model. p. 1-16. In *Three-Dimensional Coastal Ocean Models*, ed. by N. Heaps, AGU, Washington D.C..

Carter, G. S., M. A. Merrifield, J. M. Becker, K. Katsumata, M. C. Gregg, D. S. Luther, M. D. Levine, T. J. Boyd and Y. L. Firing (2008): Energetics of M_2 barotropic-to-baroclinic tidal conversion at the Hawaiian Islands. *J. Phys. Oceanogr.*, **38**, 10, 2205-2223.

Decloedt, T. and D. S. Luther (2010): On a simple empirical parameterization of topography-catalyzed diapycnal mixing in the abyssal ocean. *J. Phys. Oceanogr.*, **40**, 3, 487-508.

Egbert, G. D. and R. D. Ray (2000): Significant dissipation of tidal energy in the deep ocean inferred from satellite altimeter data. *Nature*, **405**, 6788, 775-778.

Ferrari, R. and C. Wunsch (2009): Ocean circulation kinetic energy: reservoirs, sources and sinks. *Annu. Rev. Fluid Mech.*, **41**, 253-282.

Furuichi, N., T. Hibiya and N. Niwa (2008): Model-predicted distribution of wind-induced internal wave energy in the world's oceans. *J. Geophys. Res.*, **113**, C09034, doi:10.1029/2008JC004768.

Hasumi, H. and N. Suginohara (1999): Effects of locally enhanced vertical diffusivity over rough bathymetry on the world ocean circulation. *J. Geophys. Res.*, **104**, C10, 23367-23374.

Iwamae, N., T. Hibiya and M. Watanabe (2009): Numerical study of the bottom-intensified tidal mixing using an "eikonal approach". *J. Geophys. Res.*, **114**, C05022, doi:10.1029/2008JC005130.

Jayne, S. R. and L. C. S. Laurent (2001): Parameterizing tidal dissipation over rough topography. *Geophys. Res. Lett.*, **28**, 5, 811-814.

Kantha, L. H. and C. C. Tierney (1997): Global baroclinic tides. *Prog. Oceanogr.*, **40**, 163–178.

Kuhlbrodt, T., A. Griesel, M. Montoya, A. Levermann, M. Hofmann and S. Rahmstorf (2007): On the driving processes of the Atlantic meridional overturning circulation. *Rev. Geophys.*, **45**, RG2001, doi:10.1029/2004RG000166.

Levitus, S. and T. P. Boyer (1994): World Ocean Atlas 1994, Vol. 4, Temperature, NOAA Atlas NESDIS 4, U. S. Dep. of Commer., Washington, D.C..

Levitus, S., R., Burgett and T. P. Boyer (1994): World Ocean Atlas 1994, Vol. 3, Salinity, NOAA Atlas NESDIS 3, U. S. Dep. of Commer., Washington, D.C..

Matsumoto, K., T., Takanezawa and M. Ooe (2000): Ocean tide models developed by assimilating Topex/Poseidon altimeter data into hydrodynamical model: a global model and a regional model around Japan. *J. Oceanogr.*, **56**, 5, 567-581.

Munk, W. (1981): Internal waves and small-scale processes. p. 264–291. In *Evolution of Physical Oceanography*, ed. By B. S. Warren and C. Wunsch, MIT Press, Cambridge, Mass.

Munk, W. H. and C. Wunsch (1998): Abyssal recipes II: energetics of tidal and wind mixing. *Deep-Sea Res. Part I*, **45**, 12, 1977-2010.

Morozov, E. G. (1995): Semidiurnal internal wave global field. *Deep Sea Res., Part I*, **42**, 1, 135–148.

Nycander, J. (2005): Generation of internal waves in the deep ocean by tides. *J. Geophys. Res.*, **106**, C10028, doi:10.1029/2004JC002487.

Niwa, Y. and T. Hibiya (2004): Three-dimensional numerical simulation of M_2 internal tides in the East China Sea. *J. Geophys. Res.*, **109**, C04027, doi:10.1029/2003JC001923.

Pacanowski, R. C. and S. G. H. Philander (1981): Parameterization of vertical mixing in numerical models of tropical oceans. *J. Phys. Oceanogr.*, **11**, 11, 1443–1451.

Schmitz, W. J. (1995): On the interbasin-scale thermohaline circulation, *Rev. Geophys.*, **33**, 2, 151–174.

Simmons, H. L., R. W. Hallberg and B. K. Arbic (2004): Internal wave generation in a global baroclinic tide model, *Deep Sea Res., Part II*, **51**, 25-26, 3043–3068.

Sjöberg, B. and A. Stigebrandt (1992): Computations of the geographical distribution of the energy flux to mixing processes via internal tides and the associated vertical circulation in the ocean, *Deep Sea Res., Part A*, **39**, 2A, 269–291.

Smith, W. H. F. and D. T. Sandwell (1997): Global sea floor topography from satellite altimetry and ship depth soundings, *Science*, **277**, 5334, 1956-1962.

St. Laurent, L. C., H. L. Simmons and S. R. Jayne (2002): Estimating tidally driven mixing in the deep ocean. *Geophys. Res. Lett.*, **29**, 2016, doi:10.1029/2002GL015633.

Webb, D. J. and N. Suginohara (2001): Vertical mixing in the ocean. *Nature*, **409**, 6816, 37-37.

Zhai, X., R. J. Greatbatch, C. Eden and T. Hibiya (2009): On the loss of wind-induced

near-inertial energy to turbulent mixing in the upper ocean. *J. Phys. Oceanogr.*, **39**, 11, 3040–3045.

Zilberman, N., J. M. Becker, M. A. Merrifield and G. S. Carter (2009): Model estimates of M_2 internal tide generation over Mid-Atlantic Ridge topography. *J. Phys. Oceanogr.*, **39**, 10, 2635–2651.

Figure Captions

Fig. 1. The whole model domain and the bathymetry. The regions including the prominent topographic features referred in the text are indicated by yellow lined squares. The thick white line indicates the boundary between the open ocean and the coastal and marginal seas.

Fig. 2. (a) The depth-integrated kinetic energy of the semidiurnal (M_2 and S_2) internal tide. (b) As in (a) but for the diurnal (K_1 and O_1) internal tide. The results of the numerical simulation for a horizontal grid spacing of 1/15˚ are shown.

Fig. 3. (a) The depth-integrated energy conversion rate from the surface tide to internal tides for the semidiurnal (M_2 and S_2) tidal constituents. (b) As in (a) but for the diurnal (K_1 and O_1) tidal constituents. The results of the numerical simulation for a horizontal grid spacing of 1/15˚ are shown.

Fig. 4. Plots of the globally integrated energy conversion rate from the surface tide to internal tides for the major four tidal constituents (M_2, S_2, K_1 and O_1) on a logarithm scale against the horizontal grid spacing for each of the numerical simulations. The least squares fitted line is shown.

Fig. 5. Plots of the globally integrated power of the bottom topography slope on a logarithm scale against the horizontal grid spacing for each of the numerical simulations. The least squares fitted line is shown.

Fig. 6. (a) The depth-integrated dissipation rate of the internal tide energy for the semidiurnal (M_2 and S_2) tidal constituents. (b) As in (a) but for the diurnal (K_1 and O_1) tidal constituents. The results of the numerical simulation for a horizontal grid spacing of 1/15° are shown.

Fig. 7. The cumulative depth distribution of the dissipation rate of internal tide energy for the four major tidal constituents (M_2, S_2, K_1 and O_1) within the open ocean (solid lines) and within the coastal and marginal seas (dotted lines) which are calculated assuming an exponential vertical structure function with various scale height parameters ζ=10m,100m, 500m and 1000m. Note that each dissipation rate is normalized by the globally integrated baroclinic conversion rate. The boundary between the open ocean and the coastal and marginal seas is shown by the thick white line in Figure 1.

Fig. 8. Schematic diagram showing the global tidal energy budget estimated in the present study.

Table 1. The globally integrated energy conversion rate from the surface tide to internal tides obtained from each of the numerical simulations with various horizontal grid spacings, together with that obtained from the extrapolation in the limit of zero grid spacing.

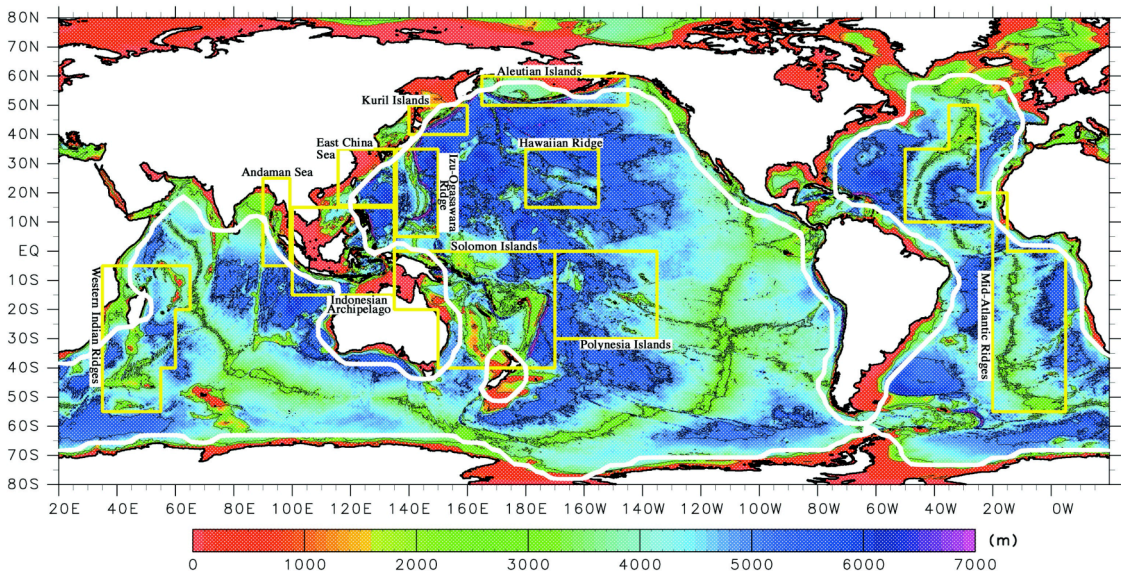
80N
70N
60N
50N
40N
30N
20N
10N
EQ
10S
20S
30S
40S
50S
60S
70S
80S
20E
40E
60E
80E
100E
120E
140E
160E
180E
160W
140W
120W
100W
80W
60W
40W
20W
0W
Aleutian Islands
Kuril Islands
East China Sea
Andaman Sea
Izu-Ogasawara Ridge
Hawaiian Ridge
Solomon Islands
Indonesian Archipelago
Polynesia Islands
Western Indian Ridges
Mid-Atlantic Ridges
(m)
0
1000
2000
3000
4000
5000
6000
7000

Figure 1

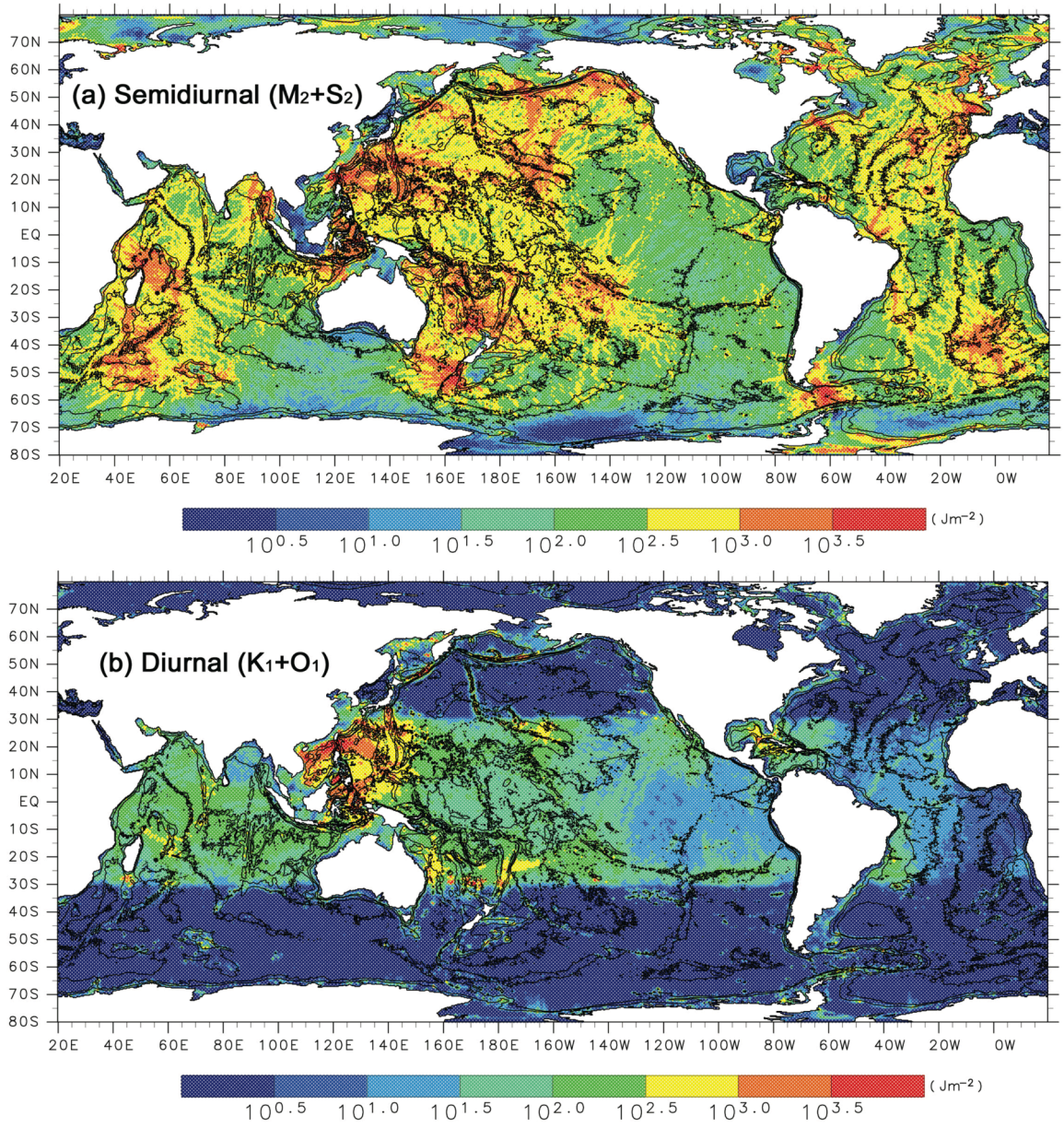
(a) Semidiurnal (M2+S2)
70N
60N
50N
40N
30N
20N
10N
EQ
10S
20S
30S
40S
50S
60S
70S
80S
20E 40E 60E 80E 100E 120E 140E 160E 180E 160W 140W 120W 100W 80W 60W 40W 20W 0W
(Jm-2)
10^0.5 10^1.0 10^1.5 10^2.0 10^2.5 10^3.0 10^3.5
(b) Diurnal (K1+O1)
70N
60N
50N
40N
30N
20N
10N
EQ
10S
20S
30S
40S
50S
60S
70S
80S
20E 40E 60E 80E 100E 120E 140E 160E 180E 160W 140W 120W 100W 80W 60W 40W 20W 0W
(Jm-2)
10^0.5 10^1.0 10^1.5 10^2.0 10^2.5 10^3.0 10^3.5

Figure 2

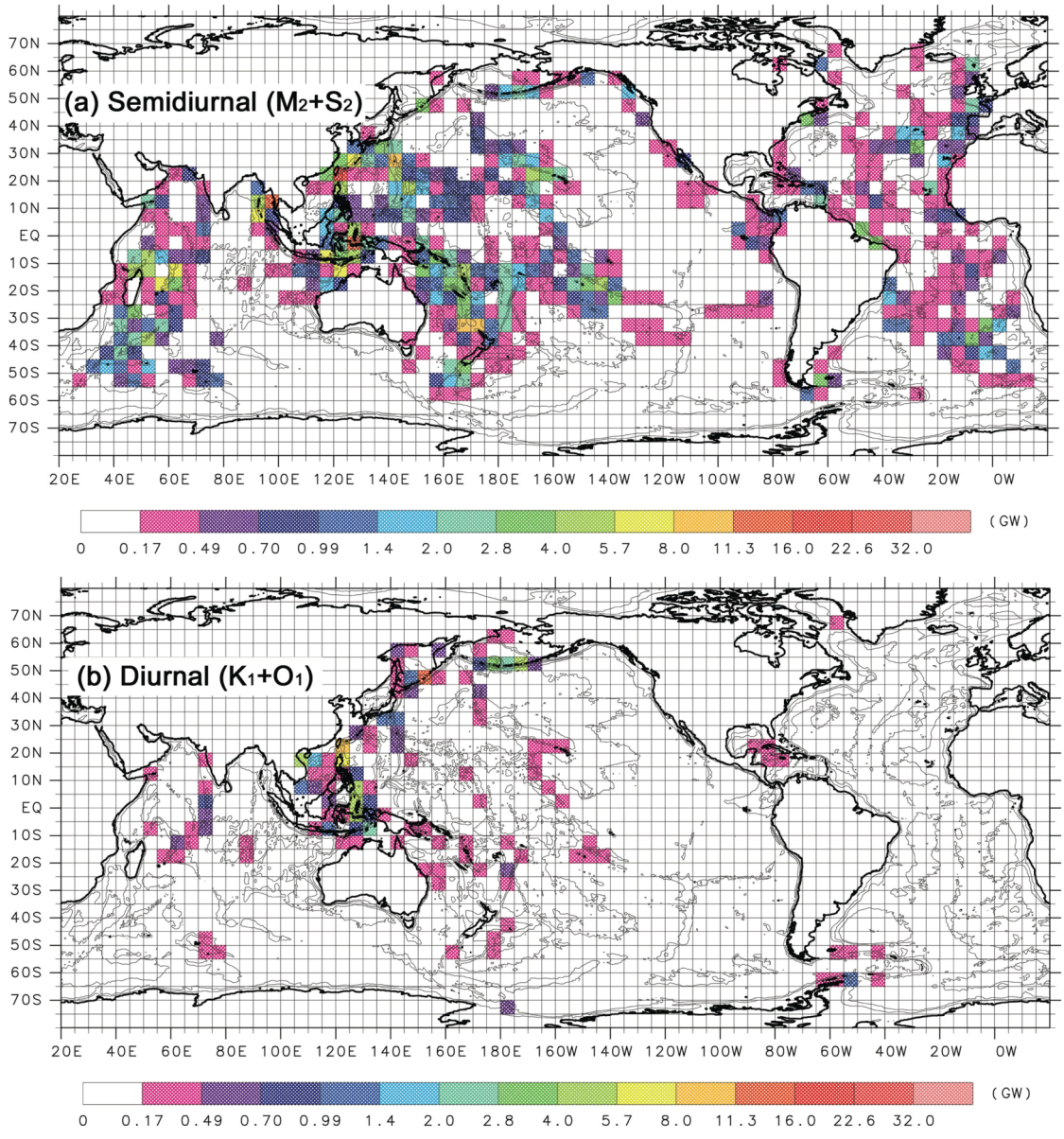
(a) Semidiurnal (M2+S2)
70N
60N
50N
40N
30N
20N
10N
EQ
10S
20S
30S
40S
50S
60S
70S
20E 40E 60E 80E 100E 120E 140E 160E 180E 160W 140W 120W 100W 80W 60W 40W 20W 0W
(GW)
0 0.17 0.49 0.70 0.99 1.4 2.0 2.8 4.0 5.7 8.0 11.3 16.0 22.6 32.0
(b) Diurnal (K1+O1)
70N
60N
50N
40N
30N
20N
10N
EQ
10S
20S
30S
40S
50S
60S
70S
20E 40E 60E 80E 100E 120E 140E 160E 180E 160W 140W 120W 100W 80W 60W 40W 20W 0W
(GW)
0 0.17 0.49 0.70 0.99 1.4 2.0 2.8 4.0 5.7 8.0 11.3 16.0 22.6 32.0

Figure 3

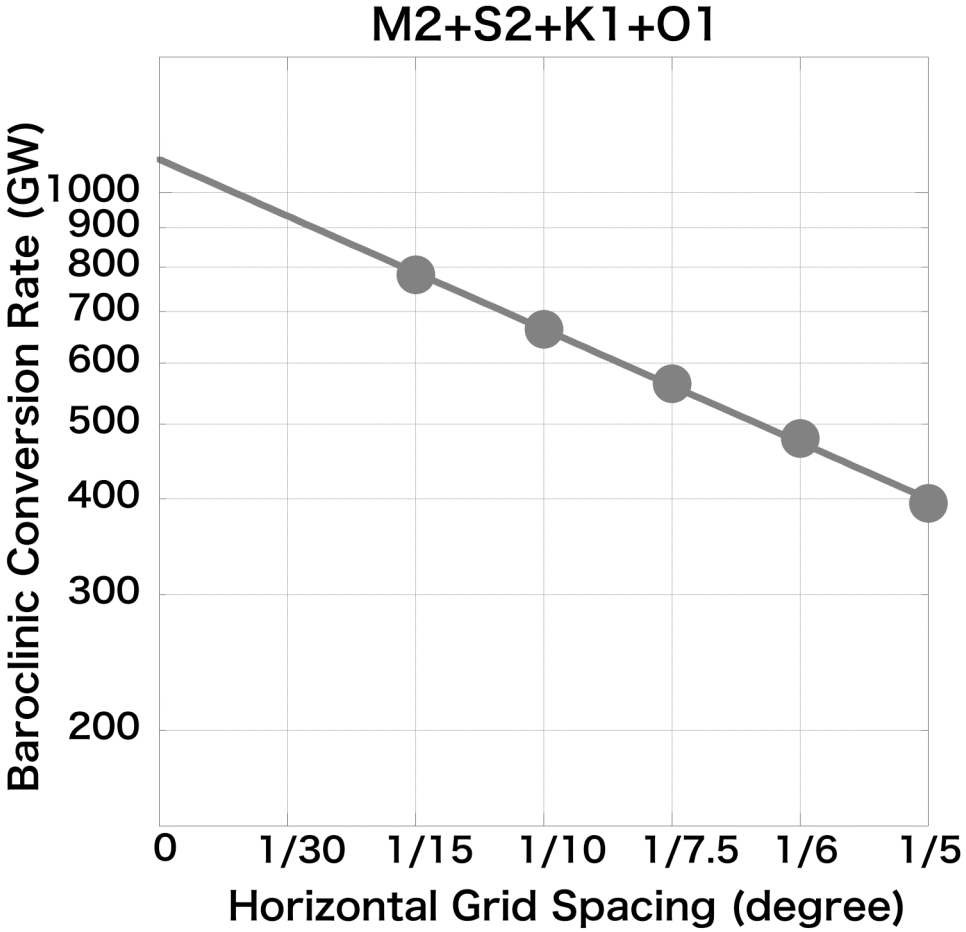
M2+S2+K1+O1
Baroclinic Conversion Rate (GW)
1000
900
800
700
600
500
400
300
200
0
1/30
1/15
1/10
1/7.5
1/6
1/5
Horizontal Grid Spacing (degree)

Figure 4

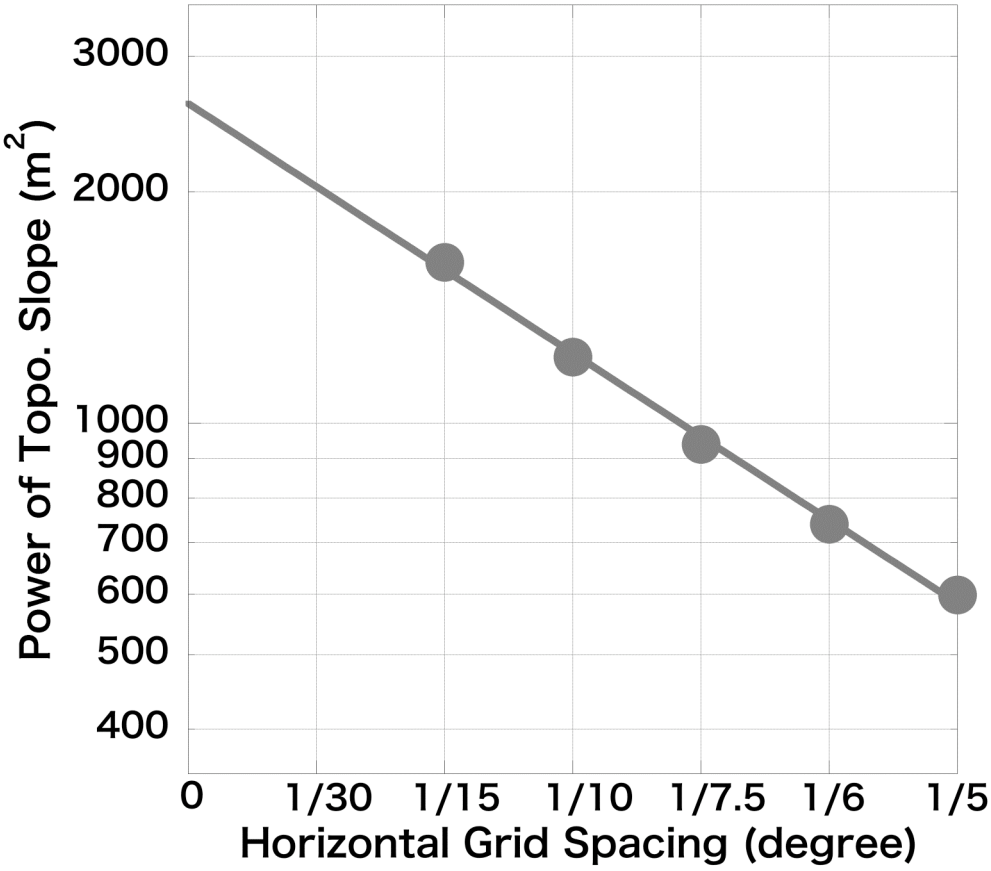
3000
2000
1000
900
800
700
600
500
400
Power of Topo. Slope (m2)
0
1/30
1/15
1/10
1/7.5
1/6
1/5
Horizontal Grid Spacing (degree)

Figure 5

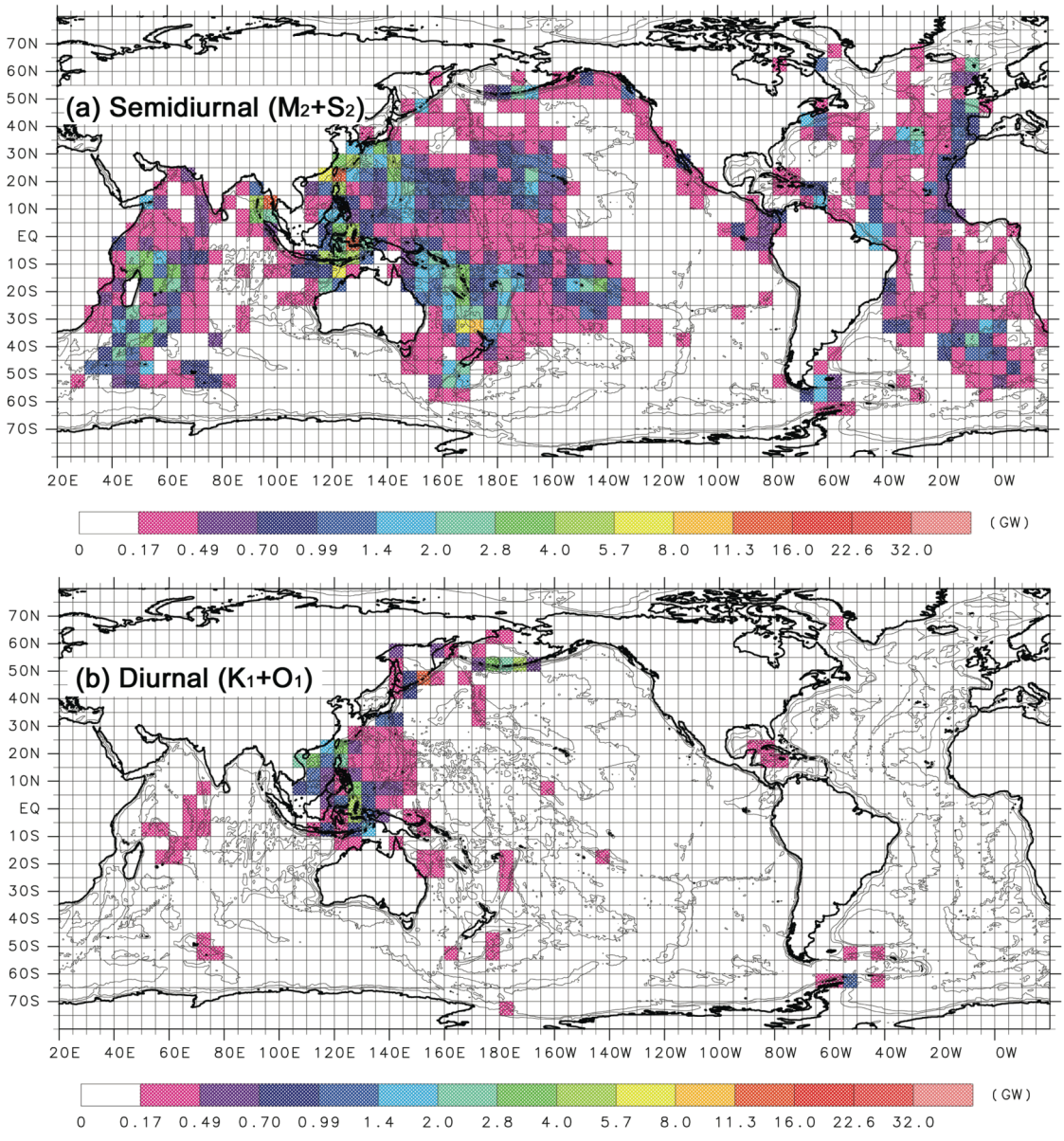
(a) Semidiurnal (M2+S2)
70N
60N
50N
40N
30N
20N
10N
EQ
10S
20S
30S
40S
50S
60S
70S
20E 40E 60E 80E 100E 120E 140E 160E 180E 160W 140W 120W 100W 80W 60W 40W 20W 0W
(GW)
0 0.17 0.49 0.70 0.99 1.4 2.0 2.8 4.0 5.7 8.0 11.3 16.0 22.6 32.0
(b) Diurnal (K1+O1)
70N
60N
50N
40N
30N
20N
10N
EQ
10S
20S
30S
40S
50S
60S
70S
20E 40E 60E 80E 100E 120E 140E 160E 180E 160W 140W 120W 100W 80W 60W 40W 20W 0W
(GW)
0 0.17 0.49 0.70 0.99 1.4 2.0 2.8 4.0 5.7 8.0 11.3 16.0 22.6 32.0

Figure 6

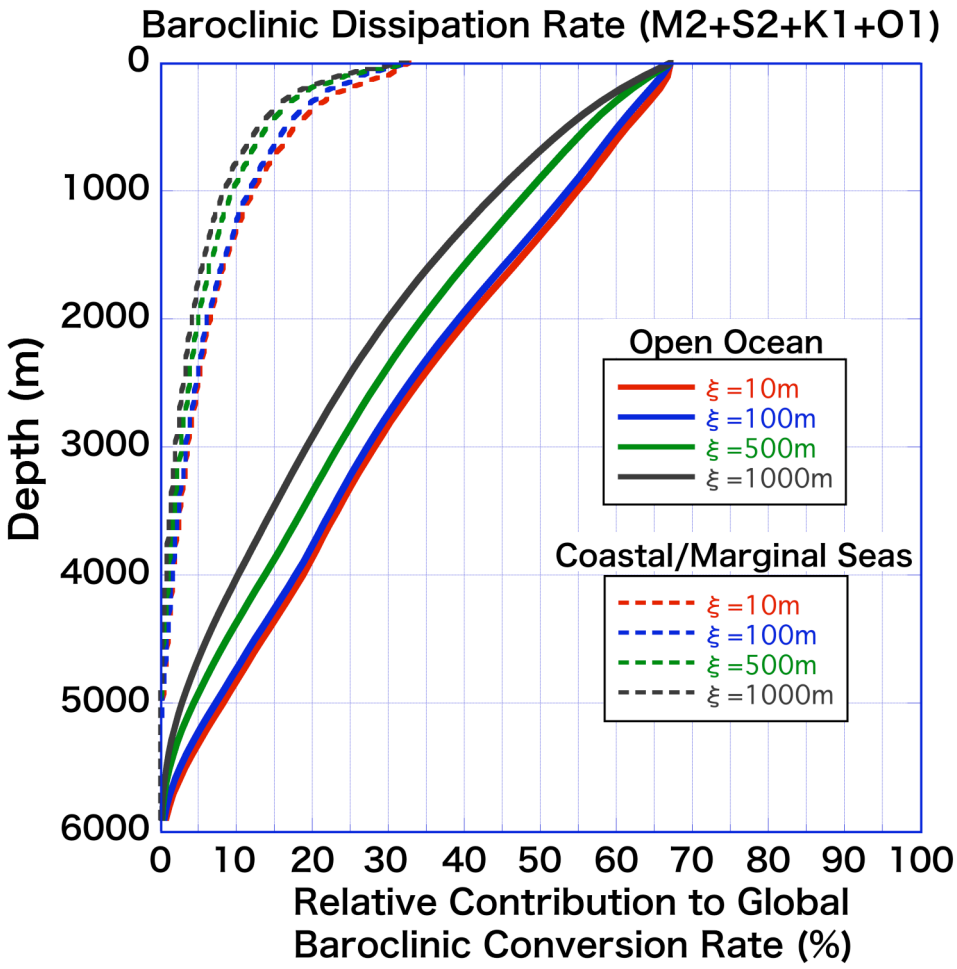
Baroclinic Dissipation Rate (M2+S2+K1+O1)
Depth (m)
0
1000
2000
3000
4000
5000
6000
0 10 20 30 40 50 60 70 80 90 100
Relative Contribution to Global
Baroclinic Conversion Rate (%)
Open Ocean
ξ =10m
ξ =100m
ξ =500m
ξ =1000m
Coastal/Marginal Seas
ξ =10m
ξ =100m
ξ =500m
ξ =1000m

Figure 7

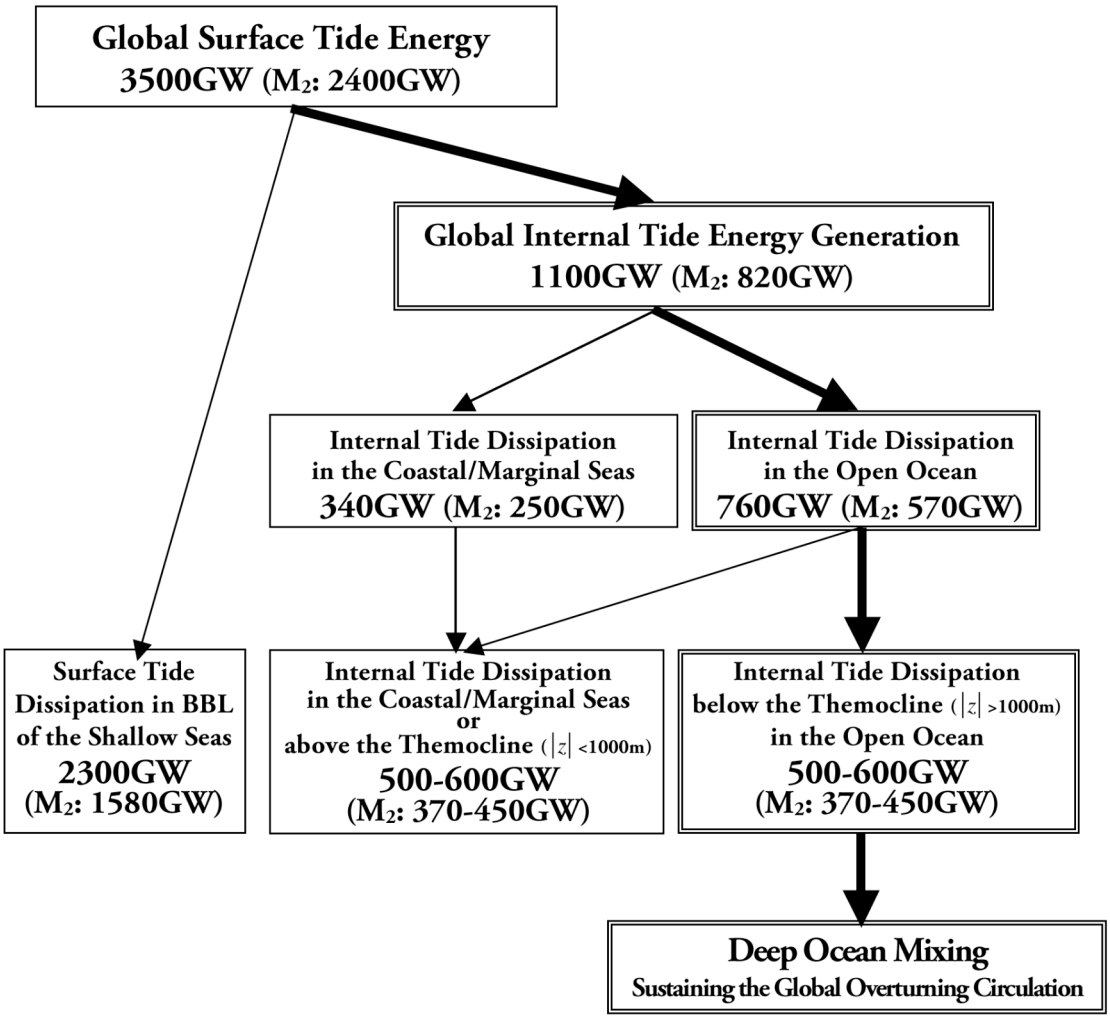
Global Surface Tide Energy
3500GW (M2: 2400GW)
Global Internal Tide Energy Generation
1100GW (M2: 820GW)
Internal Tide Dissipation
in the Coastal/Marginal Seas
340GW (M2: 250GW)
Internal Tide Dissipation
in the Open Ocean
760GW (M2: 570GW)
Surface Tide
Dissipation in BBL
of the Shallow Seas
2300GW
(M2: 1580GW)
Internal Tide Dissipation
in the Coastal/Marginal Seas
or
above the Themocline (|z| <1000m)
500-600GW
(M2: 370-450GW)
Internal Tide Dissipation
below the Themocline (|z| >1000m)
in the Open Ocean
500-600GW
(M2: 370-450GW)
Deep Ocean Mixing
Sustaining the Global Overturning Circulation

Figure 8

Horizontal Grid Spacing (degree)	Global Baroclinic Conversion Rate (GW)				
	M_2	S_2	K_1	O_1	Sum of M_2,S_2,K_1 and O_1
Δx=1/ 5	255	43	63	34	394
Δx=1/ 6	322	53	67	36	479
Δx=1/7.5	387	65	73	39	564
Δx=1/10	463	79	80	42	665
Δx=1/15	553	96	87	46	782
	Extrapolated Global Baroclinic Conversion Rate at Δx=0 (GW)				
Δx=0	821±53	145±4	102±2	53±1	1105±39

Table 1